ZIBELINE INTERNATIONAL PUBLISHING

ISSN: 2521-0920 (Print)
ISSN: 2521-0602 (Online)
CODEN: MJGAAN

Malaysian Journal of Geosciences (MJG)

DOI: http://doi.org/10.26480/mjg.02.2021.41.50

REVIEW ARTICLE

TRANSVERSE ISOTROPIC CRUST STRUCTURE BENEATH THE NORTHWEST AND CENTRAL NORTH ANATOLIA REVEALED BY SEISMIC SURFACE WAVES PROPAGATION

Özcan Çakır

Associate Professor, Süleyman Demirel University, Department of Geophysics, 32260 Isparta, Turkey.
****Corresponding Author E-mail: ozcancakir@sdu.edu.tr***

ARTICLE DETAILS

Article History:

Received 20 July 2021
Accepted 24 August 2021
Available online 10 September 2021

ABSTRACT

The Anatolian crust, which is abnormally hot, is widely deformed by subduction related volcanism. Suture zones, transform faults, thrusts and folds and metamorphic core complexes add to the geological complexity. Volcanic provinces such as Western, Central and Eastern Anatolia and Galatea are recognized as distinct features in the region. The middle-to-lower crust depths appear to be intruded by horizontal sills and the upper crust by vertical dykes. Both horizontal sills and vertical dykes leave anisotropic signs detected as Vertical Transverse Isotropy (VTI) that is explored by Love and Rayleigh surface wave inversions, i.e., Love-Rayleigh wave discrepancy which arises because the dykes and sills act differently against the Love and Rayleigh surface waves. The current study gives emphasis to the Northwest and Central North Anatolia utilizing both single-station and two-station tomography techniques to recover the two-dimensional group and phase speed charts from which one-dimensional dispersion inversions are implemented. The one-dimensional inversions are joined to construct the three-dimensional crust of the studied region. The shear-wave anisotropy is used to locate the anisotropy in the crust. The vertical dykes in the upper crust fit into negative VTI around -10% while the horizontal sills in the middle-to-lower crust yield positive VTI around 12%. The vertical magma flows within the vertical dykes and the horizontal magma flows within the horizontal sills contribute constructively to the anisotropy created by the special shape orientations of sills and dykes. The earthquakes hypocenter distribution and high and low speeds alongside the VTI provide significant clues to differentiate between diverse geological districts.

KEYWORDS

Anatolia, Crust, Surface Wave, Tomography, Transverse Isotropy.

1. INTRODUCTION

The crust and upper mantle system beneath the Anatolian plate and the surrounding area is complex with dipping slabs (subducted, torn and detached), pervasive felsic to mafic volcanism, metamorphic core complexes, fold and thrust belts, faults, and suture zones (Şengör and Yılmaz, 1981). The tectonic processes caused deformational strain in the crust producing anisotropic structures having the Crystallographic or Lattice Preferred Orientation (CPO or LPO), which is essentially independent of the seismic wavelength. The CPO of elastically anisotropic olivine mineral is commonly employed to study the flow pattern within the earth (Confal et al., 2018). The diffusion creep in the upper mantle and the plastic flow (dislocation slip) in the middle-to-lower crust are believed to be mechanisms leading to the CPO in the wave propagating medium (Miyazaki et al., 2013; Mainprice and Nicolas, 1989).

Statistical allocation of mineral CPOs in the mineral aggregate, grain nature and allocation, grain edge allocation and disorientation within grain accumulate, which are the circumstances defining the rock micro-fabric, dictate the seismic velocity and its directional dependence when dynamic recrystallization texture occurs (Wenk et al., 1997). Different CPO may develop from one mineral to another. For instance, plagioclase and alkali feldspar and mica and clay minerals show high *P* and *S*-wave anisotropy greater than 50% as single-crystal, but plagioclase and alkali feldspar minerals are known to show weak CPOs while mica and clay minerals develop strong CPOs in rocks making them main candidates for the seismic anisotropy in the crust (Almqvist and Mainprice, 2017).

Another type of anisotropy is due to the Shape Preferred Orientation (SPO). Crustal heterogeneities such as fracture and crack systems, sills and dykes, oriented melt pockets, sheet-like melts, stack of thin layers repeating themselves with a periodicity having length scale shorter than the seismic wavelength result the SPO anisotropy (Kendall, 2000). The Anatolian crust is extensively intruded by subduction-related magmatism due to the north dipping Afro-Arabian slab in the eastern Mediterranean. This magmatic activity has produced vertical dyke formations in the upper crust and horizontal sill formations in the middle-to-lower crust leading to the SPOs (Çakır, 2018, 2019).

Quick Response Code	Access this article online	
	Website: www.myjgeosc.com	**DOI:** 10.26480/mjg.02.2021.41.50

Cite the Article: Özcan Çakır (2021). Transverse Isotropic Crust Structure Beneath the Northwest and Central North Anatolia Revealed by Seismic Surface Waves Propagation. *Malaysian Journal of Geosciences, 5(2): 41-50.*

In general terms, sills fed by dykes join to create magma chambers and plutons, which is the central device to augment the continental crust (Chanceaux and Menand, 2014). Such intrusions also increase the crustal heat above the geothermal gradient. Menand has provided a review about igneous bodies where it is reported that sills and dykes generated by consecutive and distinct pulses of magma intrusions form some large plutons inside the Earth (Menand, 2011). The three main mechanisms physically control the sill formation. The first mechanism is related to the stiffness difference where dykes halt and sills accumulate at the boundary separating the upper strong stratum from the lower weaker stratum. The second one is linked to the heterogeneous flow characteristics in the crust where sills arise within the weakest flexible zones.

The third one is due to the rotation of principal stress components ($\sigma_1 > \sigma_2 > \sigma_3$) where sills arise when the least principal stress component (σ_3) converts to upright supporting the sub-horizontal intrusions. Moreover, within the solidifying magma there exists fractional crystallization since each mineral in the magma source has its own crystallization temperature which removes early solidifying minerals from the liquid magma changing the liquid composition leading to a wide range of rock formations (Meschede and Warr, 2019). In relation to the latter case, there exists viscous flow in the magma melt where these minerals solidified with uneven crystal augmentation rates and dissimilar sizes (e.g., pyroxene, olivine, feldspar, mica, and amphibole) freely rotate to result in the SPOs. Since the crystal structure and the crystal shape are directly related, the SPO in the latter case necessitates the development of CPO (Mainprice and Nicolas, 1989).

The aim of the current study is to show that the shear-wave speed anisotropy evaluated from the seismic surface waves are effective to study the magmatic intrusions in the Anatolian crust. The data analysis technique adapted herein is also utilized in other studies in the literature (Çakır 2018, 2019; Lee et al., 2021; Alkan and Çınar, 2021). We utilize Love-Rayleigh surface wave dispersion data (fundamental mode) where single-station (or source-to-station) and two-station (or inter-station or source-to-station-pair) group speeds and two-station phase speeds are measured for the analysis. The group and phase speed curves are solved in cooperation to establish the one-dimensional (1-D) shear-wave velocity and depth profiles. The Love-Rayleigh discrepancy is obvious in the detected surface waves and is engaged to analyze the anisotropic structures under the interested area. The Vertical Transverse Isotropy (VTI), which is the simplest form of anisotropy, is effectively employed to model the current detected anisotropy largely instigated by igneous rocks, i.e., negative VTI in the upper crust and positive VTI in the middle-to-lower crust (Fu and Li, 2015). Since the principles relevant to the wave propagating medium with considered anisotropy are broadly elucidated elsewhere, the respective details are omitted here (Çakır, 2019).

The Anatolian plate is unusually hot as exposed by the prevalent geothermal activity and high heat flow detections (~110 mW/m2 – İlkışık, 1995) (Pasvanoğlu and Gültekin, 2012; Pasvanoğlu and Çelik, 2019). The seismic speeds in the crust and uppermost mantle are abnormally slower compared to a usual earth assemblage – e.g., IASP91 (Kennett and Engdahl, 1991; Delph et al., 2015; Çakır, 2018, 2019). Çakır and Erduran have utilized teleseismic *P* and *S* receiver functions to study the 1-D shear-wave velocity structure of the crust and upper mantle beneath station ANTO (near central Anatolia) where they have detected a shallow Lithosphere–Asthenosphere Boundary – LAB at ~70-km depth and a Low Velocity Zone – LVZ atop the 410-km discontinuity (Çakır and Erduran, 2011). A group researcher has analyzed teleseismic *S* receiver functions to determine the lithosphere thickness underneath the Anatolian plate (Kind et al., 2015). They have predicted shallow LAB in the depth range 80-100 km and a velocity reversal (i.e., LVZ) above the 410-km discontinuity, which was interpreted as a zone of partial melt. A group researcher has reported that the shear wave (S_n) attenuation relatively strong in the asthenosphere underlying the shallow lithosphere probably resulted from partially molten asthenosphere (Gök et al., 2003). The above results are interpreted as resulting from the detachment of the Afro-Arabian slab alongside uprising buoyant asthenosphere (Keskin, 2003; Biryol et al., 2011; Portner et al., 2018).

There exist few geophysical studies to delineate the seismic crust assemblage underneath the Northwest and Central North Anatolia (Yolsal-Çevikbilen et al., 2012; Licciardi et al., 2018). On the other hand, the tectonic growth of Anatolia was subject to many seismological studies (Bakırcı et al., 2012; Warren et al., 2013). Few studies exist employing the Love and Rayleigh surface waves to inspect the VTI crust formation below Anatolia (Çubuk-Sabuncu et al., 2017; Çakır, 2018, 2019). The current study affords important evidence about the depth distribution of crustal magmatic rocks (i.e., sills and dykes) beneath the Northwest and Central North Anatolia, which is not reported elsewhere. The horizontal sills are emplaced in the middle-to-lower crust and the vertical dykes in the upper crust. The findings related to the shear-wave speeds may help us determine if these sill bodies are already cooled (i.e., high speed zones) or still cooling (i.e., low speed zones).

There are several accelerometer and broadband stations in the study area, which have been continuously recording earthquakes since year 2010 (accelerometer stations) and year 2006 (broadband stations). We take the advantages of these recordings until year 2020 to invert the surface waves for the determination of underground structure (shear-wave speed and anisotropy). Both group and phase speeds of fundamental mode surface waves are concurrently employed in the inversion. The Love and Rayleigh dispersion curves are attained for the propagation pathways and then these dispersion curves are inverted employing a tomography procedure to accomplish the two-dimensional (2-D) dispersion curve charts. For each grid point on the 2-D dispersion curve chart we invert the corresponding dispersion data to obtain the 1-D shear-wave speed-depth profile and then combine these solutions to assemble the 3-D crust speeds under the studied area. We eventually propose crustal VTI models to elucidate the apparent Love-Rayleigh wave discrepancy.

2. Geological Setting

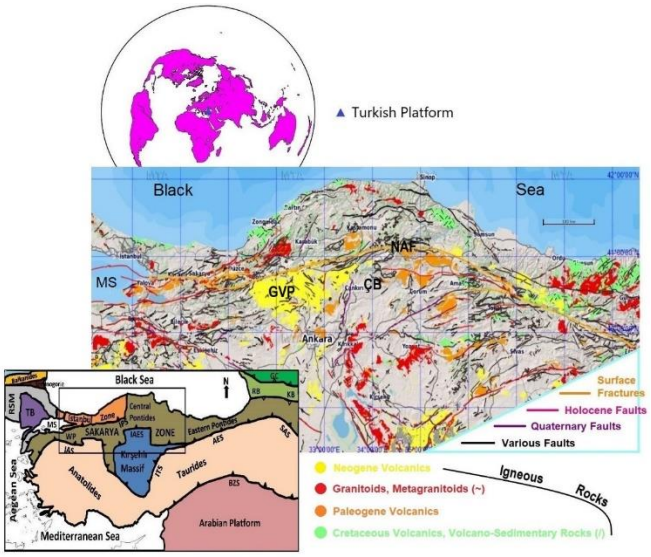

Figure 1: Basic geologic map of the Northwest and Central North Anatolia is demonstrated (adapted from MTA, 2002; also see Emre et al., 2013; Akbas et al., 2017). GVP stands for Galatean Volcanic Province, NAF for North Anatolian Fault and ÇB for Çankırı Basin. The small inset shows the Palaeotectonic assemblages in Turkey where BZS stands for Bitlis-Zagros Suture, GC for Greater Caucasus, IAES for Izmir-Ankara-Erzincan Suture, IPS for Intra-Pontide Suture, ITS for Inner-Tauride Suture, KB for Kura Basin, MS for Marmara Sea, RB for Rioni Basin, RSM for Rhodope-Strandja Massif, SAS for Sevan-Akera Suture, TB for Thrace Basin, WP for Western Pontides (modified from Okay 2008). The rectangle shows the studied area.

The studied region composed of Istanbul Zone, Central and Western Pontides, Anatolide-Tauride Platfrom and Kırşehir Massif is cut by the North Anatolian Fault – NAF and is sutured by the Ankara-Erzincan Suture – IAES (Figure 1). The NAF and the associated sub-branches extend in approximately E-W direction producing the main seismicity in the studied region as shown by the epicenters of earthquakes in Figure 2 (red color

stars – upper panel). The earthquake catalog adapted from the database of Disaster and Emergency Management Presidency (AFAD) include earthquakes with magnitude range $3.5 \leq M_w \leq 6.5$, focal depth ≤ 40 km and 29-year time span from 1990 to 2019. Some profiles are selected to examine the current findings in 2-D cross sections. These black color circles in Figure 2 (upper panel) highlight the epicenters happening closer to profiles A-A' and B-B'. Figure 2 also illustrates these important surface geological units. In Northern Anatolia, ancient ocean basins in the Tethyan convergence system between the Pontide and Anatolide–Tauride continents were subducted during the Palaeogene (Pourteau et al., 2016).

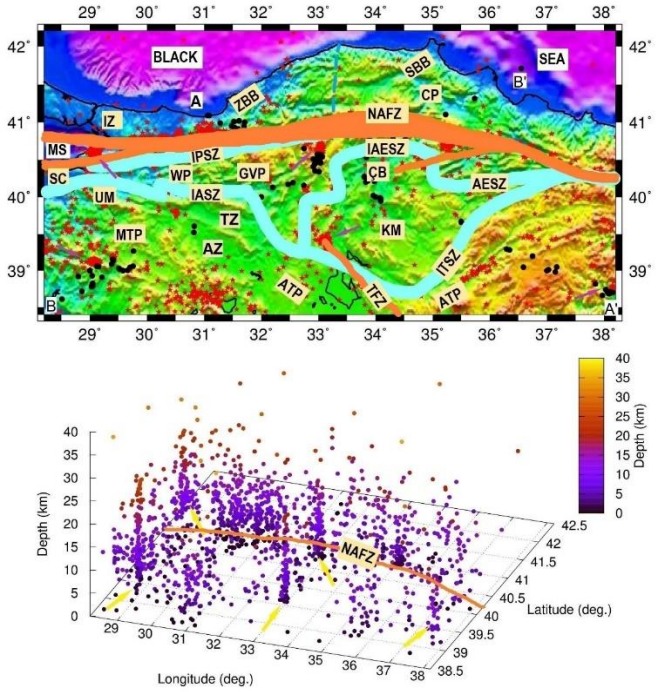

Figure 2: The seismicity in the studied area is shown by the red stars (upper panel). The seismicity represented by black circles occurs along profiles A-A' and B-B' designated in Figure 7. The principal tectonic units are marked using the following abbreviations – Afyon Zone: AZ; Anatolide-Tauride Platform: ATP; Central Pontides: CP; Çankırı Basin: ÇB; Galatean Volcanic Province: GVP; Inner-Tauride Suture Zone: ITSZ; Intra-Pontide Suture Zone: IPSZ; Istanbul Zone: IZ; Izmir-Ankara-Erzincan Suture Zone: IAESZ; Kırşehir Massif: KM; Marmara Sea: MS; Menderes-Tauride Platform: MTP; North Anatolian Fault Zone: NAFZ; Sakarya Continent: SC; Sinop-Boyabat Basin: SBB; Tavşanlı Zone: TZ; Tuzgölü Fault Zone: TFZ; Uludağ Massif: UM; Western Pontides: WP; Zonguldak-Bartın Basin: ZBB. The lower panel shows the earthquakes hypocenters as a function of latitudes and longitudes. The arrows (purple color in upper panel and yellow color in lower panel) indicate those earthquakes grouped around a certain locality.

To the west the subduction zone between the Menderes-Tauride Platform (MTP) and the Sakarya Continent (SC) is characterized by the Izmir-Ankara Suture Zone – IASZ (Okay and Tüysüz 1999). The Intra-Pontide Suture Zone – IPSZ represents a plunge zone between the Istanbul Zone – IZ and the SC (Okay and Tüysüz, 1999). To the east the subduction zone between the Central Pontides (CP) and the Anatolide–Tauride Platform (ATP) is characterized by the Ankara-Erzincan Suture Zone – AESZ while to the southeast the Inner-Tauride Suture Zone – ITSZ marks the thrust zone between the Kırşehir Massif (KM) and the ATP (Okay and Tüysüz 1999). The Çankırı basin – ÇB overlapping the Izmir-Ankara-Erzincan Suture Zone – IAESZ consists of pre-Middle Miocene sedimentary fill (>3-km thick) and is underlain by Upper Cretaceous ophiolites and granitoids of the KM (Kaymakci et al., 2009).

The Galatean Volcanic Province – GVP (Early–Middle Miocene) taking place between the IASZ and the IPSZ-NAFZ (Figure 2) comprises of dacites, andesites and pyroclastites and rhyolites and small amount of basaltic trachyandesites and trachybasalts where small magma surges or dykes are evident (Varol et al., 2014). There exist basin structures characterizing the southern Black Sea (back-arc basin) margin where the Tethys Ocean subducted below the Pontides, i.e., to the northeast the Sinop-Boyabat Basin – SBB and to the northwest the Zonguldak-Bartın Basin – ZBB (Hippolyte et al., 2016). Some researchers have reported that the Tavşanlı Zone – TZ reveals the high-pressure low-temperature (HP–LT) metamorphism (e.g., blueschist facies) to the south of the IASZ where a remnant subduction edge evolving from early obduction phases to continental plunge occurs and the subduction accretionary composite is squeezed between the ATP and the obducted ophiolites (non-metamorphic) (Plunder et al., 2013).

The Afyon Zone – AZ is another metamorphic zone (greenschist facies) between the TZ to the north and the Anatolides to the south comprising meta-sedimentary and meta-volcanic rocks composed of dacite, rhyolite and trachyandesite (Özdamar et al., 2013). The Uludağ Massif – UM is an exhumed mountain range consisting of high-grade metamorphic (amphibolite-facies gneiss, marble, and amphibolite) and intrusive early Eocene granitic rocks (Topuz and Okay, 2017). The Tuzgölü Fault Zone – TFZ creates significant seismicity in central Anatolia along mostly dip slip and partly right-lateral strike slip motions (Yıldırım, 2014). The lower panel in Fig. 2 displays the regional earthquake hypocenters in 3-D where some earthquakes with focal depth as deep as 40 km show four distinct groups (pointed by yellow arrows in lower panel and by purple arrows in upper panel) clustering in a narrow window of latitudes and longitudes, which might be due to earthquakes caused by active magmatic intrusions in the region.

3. Materials and Methods

Modern seismic waveform data and processing techniques extensively tested and verified by the researchers are currently utilized (Tang and Zheng, 2013; Wu et al., 2016; Dixit et al., 2017). Minor-to-strong sized shallow earthquakes in the Anatolian plate and the surrounding area provide unique opportunity to study the seismic surface waves for the crust properties using both single-station and two-station techniques.

3.1 Waveform data from seismic stations

The Anatolian plate is densely covered by accelerometer stations. There currently exist 678 of these stations with 50 km or less distance between neighboring stations deployed by the Turkish Disaster and Emergency Management Presidency (AFAD, 2019). The studied area having the longitude range 28.2°E–38.2°E and the latitude range 38.4°N–42.2°N presently has 164 such accelerometer stations from which we attain three-component accelerograms. The recording instruments are Geosig-GMPLUS-AC-73 (47 stations), Sara-ACEBOX-SA10 (26 stations) and Guralp-CMG5TD-CMG-5T (91 stations). Some accelerometer stations have recording history going back to year 2010 while some stations have one year or less recording history contributing only one or two recordings. The accelerograms multiplied by the instrument constant are delivered in units of cm/s^2 by AFAD and the transfer function is not processed. The two instruments [i.e., CMG5TD-CMG-5T/Guralp (GURALP, 2013) and GMPLUS-AC-73/Geosig (GEOSIG, 2012; also, personal message)] have flat response with zero-degree phase shift and zero dB amplitude gain from dc to at least 10 Hz. The instrument (i.e., ACEBOX-SA10/Sara) has two different transfer functions for operation dates before and after 07 April 2017 for which we employ the related pole-zero files distributed by the instrument supplier (SARA, 2017; also, personal contact).

The Anatolian plate has also hundreds of three-component broadband seismic stations operated by Kandilli Observatory and Earthquake Research Institute (KOERI). We employ 54 of these stations taking place in the studied area. There are also other waveform data resources that we utilize; i.e., 39 broad-band stations installed and operated by the project "North Anatolian Fault (NAF) Passive Seismic Experiment" in the time period from January 2006 to May 2008, 62 broad-band stations installed and operated in a temporary array "Dense Array for Northern Anatolia – DANA" with a station spacing of ~7 km in the time period from May 2012 to October 2013 and 72 broad-band stations installed and operated by the

project "Continental Dynamics: Central Anatolian Tectonics – CDCAT" in the time period from May 2013 to May 2015 where 13 stations among the CDCAT stations having locations relevant to this work are employed herein (Özacar et al., 2006; Kahraman et al., 2015; Abgarmi et al., 2017). The pole-zero files corresponding to each broadband station are used to remove the effect of seismometer response.

For the single-station surface wave analysis the regional earthquakes occurred within the borders of the interested area were scanned from year 2005 to year 2019 where the event search resulted 709 earthquakes with magnitude $M_w \geqslant 3.5$. The waveforms were visually selected among which 365 events satisfied our selection criteria. Generally, the handpicked earthquakes have the magnitude band $3.5 \leqslant M_w \leqslant 5.7$ and the focal depth interval $0.4 \leqslant h \leqslant 46.11$ km. The source constraints (i.e., epicenter location, date, origin time, magnitude, depth) of the earthquakes that we utilize are adopted from the AFAD collection, which is also validated with the EMSC (European-Mediterranean Seismological Centre) and USGS (United States Geological Survey) catalogs. The E-W and N-S accelerograms are rotated into the Transverse and Radial accelerograms using the theoretical back-azimuth and are converted into the particle velocity by means of the traditional integration. The Love surface wave data is obtained from the transverse component and the Rayleigh surface wave data from the vertical component. The observed waveforms are band-pass filtered in the period band 5-20 s.

For the two-station surface wave analysis those earthquakes with magnitudes $M_w \geqslant 4.1$ occurred in the same time interval (years 2005-to-2019) outside the interested area were also scanned where this event search resulted 942 earthquakes. The surface wave energy is attenuated with distance and this attenuation increases with decreasing wavelength. The epicentral distance range of the two-station events is selected to be <3000 km so that at least 10-s (if not 5-s) period surface waves are existent on the recordings surviving through the attenuation along the propagation distance. The waveforms were again visually examined after which 667 events yielding effective two-station pathways fulfilled our selection measures. The handpicked earthquakes have the focal depth interval $0.9 \leqslant h \leqslant 49.9$ km and the magnitude band $4.1 \leqslant M_w \leqslant 7.3$. The resultant events are employed to attain the two-station phase and group speeds.

3.2 Multiple Filter Technique

To determine the single-station and two-station group speeds of the fundamental mode we apply the Multiple Filter Technique by means of the narrow-band Gaussian filter $\exp[-\alpha\,(f-f_c)^2/f_c^2]$ where f_c denotes the center frequency of the filter (MFT – Herrmann, 2002). The filter bandwidth is controlled by α that exchanges resolution going from time domain to frequency domain, i.e., smaller α results broader filter in the frequency domain while the time domain signal becomes shorter in duration. After some trial-and-error applications we set $\alpha = 12.5$. Smaller α (e.g., $\alpha \leqslant 6.25$) wears down the observational features of the group speed curves while larger α (e.g., $\alpha \geqslant 25$) often results in fragmented and noisy dispersion curves. In fact, the ideal α filter parameter is a function of distance and for the distances shorter than 1000 km, recommends using $\alpha = 25$ (Herrmann, 2002). We presently apply the MFT within the distance range 50-800 km. The seismic scattering, higher modes and noise interfere with the fundamental mode energy. We implement the Phase-Matched Filter to alleviate the effect of such distortions (e.g., see Çakır, 2018, 2019; PMF – Herrin and Goforth, 1977).

The definition given in Eq. (1) utilizing the cross-correlation is employed for the two-station investigation of surface waves. The source phase is excluded by taking the two stations on the same great circle pathway with the source. Some abnormality from the great circle pathway is tolerable since the great circle condition is not regularly fulfilled. The two angles (i.e., $\theta_1 \leqslant 1$ and $\theta_2 \leqslant 5$) is used to regulate the abnormality of the great circle pathway. Here the angle θ_1 measures the azimuthal change of the source to the two receivers and the angle θ_2 corresponds to the azimuthal change between the source to the first receiver and the first receiver to the second receiver. The two-station phase speed computed from the cross-correlogram in frequency domain is quantified as follows.

$$c(\omega) = \frac{\omega r}{arctan\{Imag\,[\psi(\omega)]/Real\,[\psi(\omega)]\} + 2n\pi} \quad (1)$$

In Eq. (1), the cross-correlogram is given by the complex function $\psi(\omega)$, the inter-station distance by r and the angular frequency by ω. The quantity $2n\pi$ in the denominator specifies the ambiguity in the determination of the phase speed $c(\omega)$. We work with the MFT given in Herrmann where a different control (IG) is made available to synchronously estimate the phase and group speeds from the inter-station cross-correlograms (Herrmann, 2002).

3.3 2-D Tomographic Speed Charts

We perform the 2-D speed tomography for both group and phase speeds. The single-station group speeds are obtained for each station-source pathway. The two-station group speeds are attained for each station-station pathway where the first station is treated as a source and the second station as a receiver. Rawlinson and Sambridge have provided a tomography code that we utilize to implement the 2-D speed tomography (Rawlinson and Sambridge, 2003). Supposing a constant radius and variable latitude and longitude a spherical coordinate system with 2-D spherical shell is applied to compute the travel times from point sources to receivers by solving the Eikonal equation along with a fast-marching method (FMM). The travel time model on the spherical shell is defined by bi-cubic B-spline interpolation on a grid of nodes. The association between the travel time and speed is non-linear for which a linearized inversion scheme is utilized. To prevent the non-uniqueness in the inversion, smoothing and damping controls are used. The following objective function $\phi(m)$ is iteratively solved to minimize the differences between the detected and computed travel times (Tarantola, 1987).

$$\phi(m) = [g(m)-d]^T C_d^{-1}[g(m)-d] + \sigma[m-m_o]^T C_m^{-1}[m-m_o] + \gamma m^T D^T D m \quad (2)$$

where d and $g(m)$ stand for the detected and computed travel times, respectively. The model and data covariance matrices are described by C_m^{-1} and C_d^{-1}, respectively. The damping ($\sigma = 0.75$) and smoothing ($\gamma = 1.50$) factors are effective to deter the inverted model (m) from proceeding too far from the initial model (m_o) while making the consequent model smooth where the model smoothness matrix is given by D. Eq. (2) is solved twice, i.e., first time for the group speeds and second time for the phase speeds. The speed grid is defined by a 2-D mesh size given by 0.1° x 0.1° in latitude and longitude. This corresponds to 39 mesh points along the latitude range 38.4°–42.2° and 101 mesh points along the longitude range 28.2°–38.2°, i.e., 39 × 101 = 3939 nodes designate the speed grid.

4. Inversion Results

The period dependent inversion results are presented in two sections, i.e., group speed charts and phase speed charts from which group and phase speed curves at each grid point are established for both Love and Rayleigh surface waves. These dispersion curves are then converted into 1-D shear-wave speed-depth profiles, which are collectively interpreted for the 3-D seismic image of the crust assemblage beneath the concerned area.

4.1 2-D Group Speed Charts

There are 164 accelerometer and 176 broadband recording stations, and 365 earthquakes (sources) utilized in the single-station analysis. The recording stations are also treated as sources in conjunction with the two-station analysis. Therefore, the number of sources in the single-station analysis is (164+176+365) = 705. The tomography source code requires two input files from the user. The first file includes the travel time data consisting of three columns where the first column states if there is data for the station-source pathway, the second column is the travel time and the third column is the standard error for the corresponding data. The second file includes the information regarding the locations of the receivers and sources. For each surface wave period from 5 to 20 s with 1 s interval a separate travel times file is arranged and is used in the tomographic inversion.

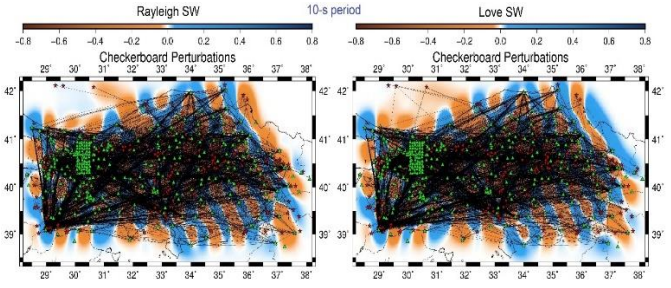

Figure 3: Group-speed checkerboard tests for the Love (right) and Rayleigh (left) waves are shown. The cell size of perturbation is 0.50° x 0.50°. The stars are source locations, and the triangles are recording seismic positions. The ray-paths are drawn using the thinnest line available in the drawing program.

The checkerboard tests outlined in Figure 3 are run to recognize the proficiency of the single-station group speeds data of Love (right panel) and Rayleigh (left panel) surface waves covering the studied area. Employing the smoothing and damping factors (i.e., $\gamma = 1.50$ and $\sigma = 0.75$) this test simulates the surface wave propagation adopting the receiver-source distribution obtained from the actual data. The checkerboard model has perturbations (±0.8 km/s) overlaid on the background medium with a constant speed (i.e., 2.8 km/s). The ray-paths representing the surface waves at 10-s period are superimposed on the solution model along with stars (sources) and triangles (stations). Note that some locations show the stars overlaid by the triangles at which locations we have two-station group speed contributions as well. Both Rayleigh and Love checkerboard tests reveal that the ray-path coverage is enough to reasonably restore these earth assemblies with the cell dimension of 0.50° x 0.50°. However, there exists some resolution loss towards the edges of the studied region. There is still some smearing of the checkerboard patterns particularly to the east-southeast and these high and low speed perturbations particularly in the border region are not determined well. In the following, we work with the well-determined region away from the edges.

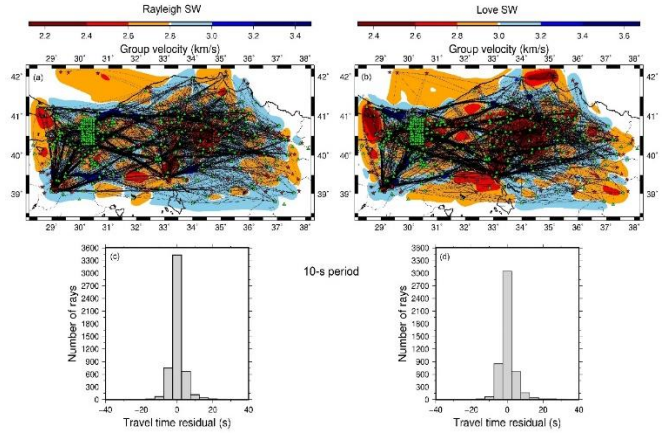

Figure 4: 2-D group-speed tomography of the detected Love (b) and Rayleigh (a) waves (10-s period). The triangles are recording positions and the stars are source locations. The frequency histograms for the Love (d) and Rayleigh (c) waves show the travel time misfit of the solution model. Both single-station and two-station recording geometries are used.

The real group travel times data acquired from the Love and Rayleigh surface waves with 10-s period are inverted in the next step. Figure 4 displays the conforming 2-D tomographic group speed charts achieved in 10 iterations. For the appropriate speed assemblage (or the background medium) we assign the constant group speed at 3.0 km/s for the Love surface waves (Figure 4b) and 2.8 km/s for the Rayleigh surface waves (Figure 4a). The white color regions in Figures 4a and 4b correspond to these regions not resolved by the existing surface waves. The orange and red color regions identify group speeds slower than the assumed background speed while these blue color tones identify the faster regions. These regions matching the Galatean Volcanic Province (GVP) and the fracture zones of the North Anatolian Fault (NAF) are mostly characterized by the slower surface wave group speeds (see Figure 2). These other regions associated with the Çankırı Basin (ÇB), Marmara Sea (MS), Sinop-Boyabat Basin (SBB) and Zonguldak-Bartın Basin (ZBB) commonly transmit slower surface waves. Away from the above regions the surface waves are generally faster, i.e., Kırşehir Massif (KM) and perhaps part of Izmir-Ankara-Erzincan Suture Zone (IAESZ).

The concluding model (10-s period) resolves most of the detected group travel times, but there exist some poorly resolved travel times as revealed by the frequency histograms shown in Figures 4c and 4d. The Rayleigh surface wave rays traversing the studied area amount to 5090 (Figure 4c) and the sum of rays for the Love surface waves is 4961 (Figure 4d). Figure 4d illustrates that 62% of the Love group travel times are resolved with residuals in the interval $-2.5 \leqslant T_{res} \leqslant 2.5$ s. The upper 17% has the residuals in the interval $-7.5 \leqslant T_{res} < -2.5$ s and the lower 14% has the residuals in the interval $2.5 < T_{res} \leqslant 7.5$ s. The remaining 7% are resolved with larger residuals (s). For the 10-s Rayleigh group travel times analogous residuals are valid as displayed in Figure 4c. It is preferable that the detected data is largely resolved by the concluding model so that the mentioned residuals stay smaller, but the ambient noise factor that we attempt to pacify in the data assessment still causes some disturbance.

The effect of the source phase on the two-station group speed estimation is alleviated through the cross-correlation procedure, but this influence persists on the single-station estimation. Therefore, errors in the determination of source parameters (i.e., location and source time) effective through the source radiation patterns may lead to erroneous group speed estimations (Çakır and Erduran, 2001). To restrict the earthquake misplacement and source time errors we have utilized three source catalogs (i.e., AFAD, EMSC and USGS). Additionally, complex wave propagation effects such as refraction, multi-pathing and scattering probably generate off-azimuth arrivals from various geological assemblages with diverse borders (e.g., Kırşehir Massif, Izmir-Ankara-Erzincan Suture, Istanbul Zone). The above noise conditions have caused some poorly resolved group travel times with larger residuals, but the percentage of such errors in the data set is small, i.e., less than 7%. For the other surface wave periods in the range 5-20 s we conducted equivalent group speed tomographic inversions like these in Figure 4.

4.2 2-D Phase Speed Charts

It is mentioned above that there are 667 earthquakes producing two-station phase speeds at (164+176) = 340 recording stations. In a similar manner to the group speed analysis described in the above subsection, we perform the phase speed tomographic inversions. The checkerboard tests sketched in Figure 5 [using the same smoothing and damping factors (i.e., $\gamma = 1.50$ and $\sigma = 0.75$) and accepting the receiver-source spreading taken from the real data] are used to check the tomographic ability of the two-station phase speeds data of Love (right panel) and Rayleigh (left panel) surface waves. Note that there exist stations (green triangles) not involved in any of the present (10-s period) two-station pathways and that the first station close to the earthquake is marked by a red star overlaid by a green triangle.

The earthquake locations mostly outside the figure frame are not shown in Figure 5. The checkerboard model is represented by perturbations (±0.8 km/s) superimposed on the propagating medium with a constant speed (i.e., 2.8 km/s). The earth assemblages with the cell dimension of 0.65° x 0.65° are satisfactorily resolved by both Rayleigh and Love surface wave phase speeds as displayed by the checkerboard tests using the real ray-path coverage. On the other hand, there is some smearing on the checkerboard patterns particularly to the west and towards the region limits the resolution gets weaker that we circumvent. The group speed tomography has better ray-path coverage than that of the phase speed tomography (i.e., compare Figures 3 and 5).

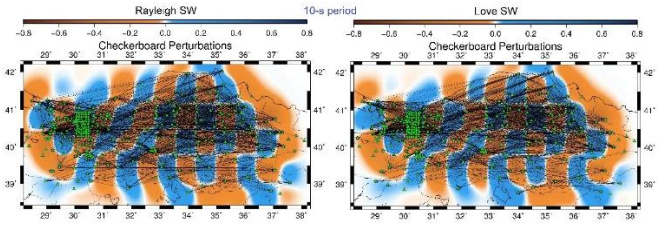

Figure 5: Phase-speed checkerboard tests for the Love (right) and Rayleigh (left) waves are shown. The cell size of perturbation is 0.65° x 0.65°. The stars are source locations, and the triangles are recording positions.

The real phase travel times data derived from the Love and Rayleigh surface waves at 10-s period are inverted in 10 iterations as shown by the 2-D tomographic phase speed charts in Figure 6. The constant phase speed at 3.4 km/s (Figure 6b) is assigned for the Love surface waves to represent the appropriate speed assemblage (or the background medium). The background phase speed for the Rayleigh surface waves is accepted as 3.2 km/s (Figure 6a). There exist some regions not resolved by the present surface waves, i.e., these white color regions in Figures 6a and 6b. The color palette used in the group speed tomography above is similarly used for the phase speed tomography. When compared to the group speed tomography (Figure 4), the phase speed tomography (Figure 6) shows somewhat smoother 2-D speed variations.

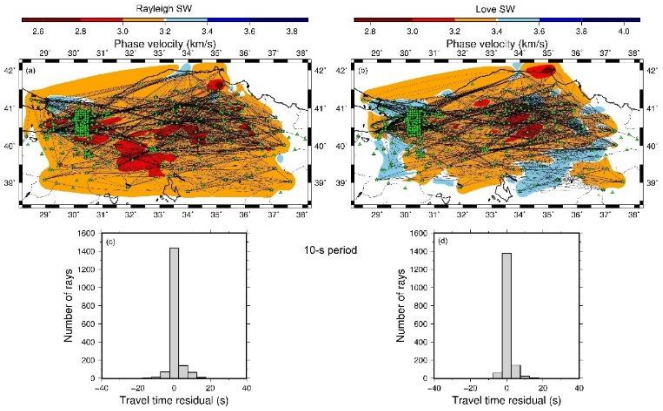

Figure 6: 2-D phase-speed tomography of the detected Love (b) and Rayleigh (a) waves (10-s period). The triangles are recording positions and the stars are source locations. The frequency histograms for the Love (d) and Rayleigh (c) waves show the travel time misfit of the solution model. Because two-station recording geometry is used, recording positions and source locations may coincide.

The GVP and the fracture zones of the NAF are characterized by the slower surface waves, which is particularly evident on the Rayleigh surface wave results (Figure 6). The lower speed basin assemblages (i.e., ÇB and ZBB) except the SBB are not apparent on the 2-D phase speed tomographic charts as clearly as visualized on the group speed charts (Figure 4). The higher speed KM is clearly visible on the Love surface waves, but the IAESZ is not possible to follow on the speed charts. In this respect, it is possible to state that the group speed charts serve more detailed structure information than that provided by the phase speed charts although the latter may also be due to the differences in the ray-path coverages (again compare Figures 3 and 5).

The frequency histograms in Figures 6c and 6d illustrate how the concluding model at 10-s period elucidates the detected phase travel times. The number of rays traversing the considered area is 1757 in the case of Rayleigh surface waves (Figure 6c) and 1628 for the Love surface waves (Figure 6d). Figure 6d identifies that 85% of the Love phase travel times are resolved with residuals in the band $-2.5 \leqslant T_{res} \leqslant 2.5$ s. The upper band ($-7.5 \leqslant T_{res} < -2.5$) includes 4% of the residuals and the lower band ($2.5 < T_{res} \leqslant 7.5$) involves 9% of the residuals. The rest counts 2% of the residuals (s). Figure 6c shows that similar residuals are effective for the 10-s Rayleigh phase travel times. The detected phase travel times are typically disturbed by ambient noise that we try to avoid during the data analysis. In addition, some two-station ray-paths show slightly off-azimuth arrivals where the associated cross-correlogram is influenced by the residue source phase causing somewhat erroneous phase travel times.

4.3 Cross Section

We now move to creating the period-dependent local group and phase speed curves on a grid with size 0.1° x 0.1°. The corresponding geographical locations are marked in Figure 7 by the black dots with white dots on the center where the group and phase speed curves are concomitantly recovered. There also exist some locations marked by the black dots where the group speed curves are only available. The local Rayleigh group and phase speed curves are jointly inverted to determine the 1-D vertically polarized *S*-wave speed model (V_{sv}) of the crust and the same process is repeated on the local Love group and phase speed curves to determine the 1-D horizontally polarized *S*-wave speed model (V_{sh}). The inversion process is the damped least-squares applied to every local dispersion curve on the grid where the crust is considered as a layered half-space assemblage with 40-km depth. The following parameter is utilized to enumerate the strength of the Vertical Transverse Isotropy – VTI.

$$\eta = \frac{(V_{sh} - V_{sv})}{V_s} \quad \dots \quad V_s^2 = \frac{(2V_{sv}^2 + V_{sh}^2)}{3} \tag{3}$$

where the Voigt isotropic average *S*-wave speed is given by V_s. The VTI (η) is positive if $V_{sh} > V_{sv}$ and is negative if $V_{sv} > V_{sh}$. The details regarding the 1-D dispersion inversion strategy, the VTI system and the matters related to the inversion power and structural simplification of Love-Rayleigh surface wave data are important. On these issues, we refer to the published work in the literature. For instance, the references therein have made the respective discussions that we also follow here (Çakır, 2018, 2019). Figure 7 also presents eight profiles of which the first one (i.e., A-A') is picked to illustrate how the inverted *S*-wave speed and anisotropy change in 2-D (depth and distance) underneath the studied area.

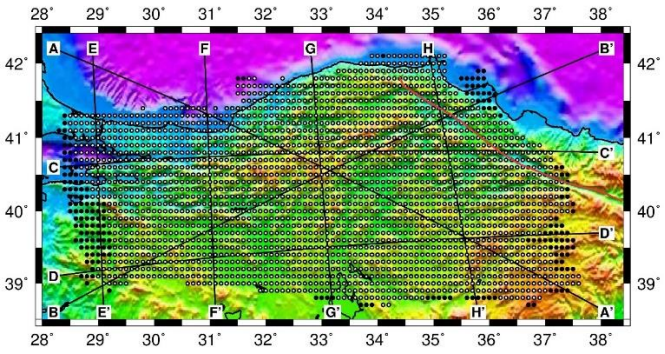

Figure 7: The eight profiles (A-A', B-B', C-C', D-D', E-E', F-F', G-G', H-H') chosen to draw some conclusions are shown. Solid circles with white dots indicate the locations of attained dispersion curves (both group and phase speeds) and solid circles specify the locations of attained group speed curves.

4.3.1 Cross Section A-A'

We show the cross section (A-A') in Figure 8 where the crust configuration in the NW-SE direction is demonstrated. A rich color scale is applied to depict the anomalies in greater detail and abbreviations for Sill (S) and Dyke (D) assemblages are used to avoid clutter in the presentation. The detected (fundamental mode) Love and Rayleigh dispersion curves (group and phase speeds) are inverted to determine the *SH*-wave (V_{sh}) and *SV*-wave speeds (V_{sv}), respectively. The Voigt isotropic average V_s speeds computed from Eq. (3) are shown in the upper panel implying that the crust assemblage below the studied area is complex in all the depth range. Above the half-space with the V_s > 4.0 km/s we have inferred five depth segments (white lines indicating irregular layer interfaces) operating on the color-coded speed-depth deviations underneath profile A-A'. The speed values approximating the V_s in each layer are listed on the right where all the layers show considerable sideways changes. Among these

layers the fourth and fifth ones from the top have the highest lateral changes with high and low speed zones. The inverted V_{sh} and V_{sv} speeds in the crust assemblage beneath profile A-A' are highly different from each other at some depth ranges pointing to the Love-Rayleigh wave discrepancy, which can be explained by the Vertical Transverse Isotropy – VTI. If the speed assemblage in the earth is isotropic, then the Love and Rayleigh wave dispersions show consistency (i.e., $V_{sh} \sim V_{sv}$).

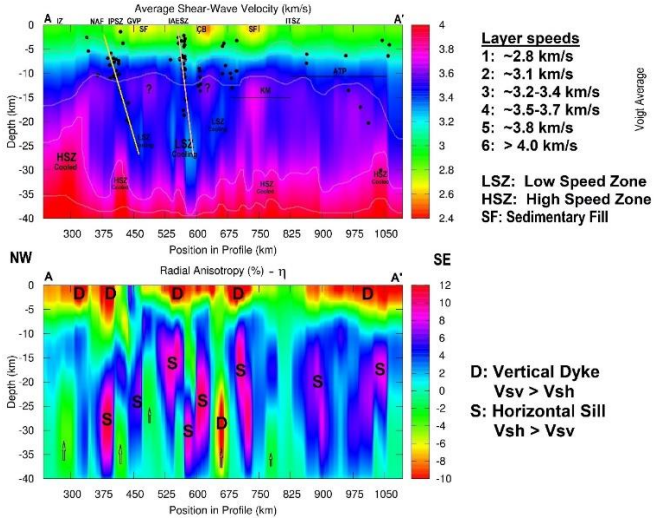

Figure 8: The inverted average S-wave speeds along with the superimposed earthquake hypocenters (upper panel) and the respective VTI (lower panel) beneath profile A-A' are illustrated. The vertical arrows in the lower panel are used to indicate likely upward magma movements with which the deep negative VTIs are associated.

The lower panel in Figure 8 presents the cross section demonstrating the VTI beneath profile A-A'. The VTI (η) computed from Eq. (3) indicates negative ($V_{sv} > V_{sh}$) and positive ($V_{sh} > V_{sv}$) anomalies where some abbreviations are used, i.e., *D* stands for the vertical dyke assemblages (negative anomalies) and *S* for the horizontal sill assemblages (positive anomalies). The upper crust is typically occupied by the negative anomalies ($\eta \sim$ -10%) and the middle-to-lower crust includes the positive anomalies ($\eta \sim$ 10%). The Love surface waves with periods shorter than ~8-s are slowed down by the vertical dyke assemblages in the upper crust (i.e., $V_{sv} > V_{sh}$). Below the dyke units the Rayleigh surface waves with periods longer than ~12-s are slowed down by the horizontal sill assemblages made of thin layers with high and low speeds in the middle-to-lower crust (i.e., $V_{sh} > V_{sv}$). Note that the negative VTI (i.e., $V_{sv} > V_{sh}$) typically overlies the positive VTI (i.e., $V_{sh} > V_{sv}$). Also note that in the upper panel, we label some depths as high-speed zone (HSZ) and low-speed zone (LSZ). If the magmatic intrusion is still cooling, then it may correspond to weakened medium where the seismic waves are decelerated (Lees, 2007). In other words, the HSZ corresponds to already cooled rocks having high strength and the LSZ correlates with still cooling rocks having low strength.

In Figure 8 (upper panel), we also show the names of the geological districts (superimposed on the V_s cross section) touching profile A-A' (NW-SE). The profile commences with the Istanbul Zone (IZ) in the NW and continues towards the SE with the North Anatolian Fault (NAF), Intra-Pontide Suture Zone (IPSZ), Galatean Volcanic Province (GVP), Izmir-Ankara-Erzincan Suture Zone (IAESZ), Çankırı Basin (ÇB) and Inner-Tauride Suture Zone (ITSZ). The Istanbul Zone (IZ) a micro-continent split from the ancient Laurasia to the north is underlain by a high-speed zone (HSZ ~3.8 km/s) in the lower crust. We interpret this HSZ with negative VTI (relatively weak around -5%) resulting from the subduction-related magmatism (already cooled) associated with the vanishing of the Intra-Pontide Ocean between the SC and the IZ in the Early Cretaceous (Akbayram et al., 2013). The NAF along which the volcanism occurs upward through the tension fractures is characterized by a few earthquakes shallower than 10-km depth around 370-km distance (Adiyaman et al., 2001). The yellow color line depicting the SE-inclined focal depths reaching 20-km depth represents the IPSZ along which the *S*-wave speed is ~3.5 km/s in the middle crust and then reverts to a low-speed zone (LSZ ~3.3 km/s) in the middle-to-lower crust. Part of the IPSZ-lower-crust around 410-km distance is perturbed by HSZ with the *S*-wave speed ~3.8 km/s raised from ~3.6 km/s. This high-speed material with negative VTI around -4% is interpreted as solidified magma emplacement surging up from the sub-Moho depths.

Again in Figure 8, the middle-to-lower crust within the IPSZ is characterized as positive VTI ~10% (i.e., horizontal sill assemblages) and the IPSZ-upper-crust reveals negative VTI (around -10%) indicative of the vertical dyke assemblages. The GVP geographically closely packed with the IPSZ, and the NAF is post-collisional associated with the trans-tensional tectonics along the NAF (Wilson et al., 1997). The assemblage under the IAESZ depicted by the pink line bears similarities to the one under the IPSZ although the respective LSZ in the middle-to-lower crust is deeper and is more pronounced with slower *S*-waves (i.e., ~3.2 km/s). Within the Çankırı Basin – ÇB the *S*-waves slow down to ~2.5 km/s from ~2.8 km/s evident in the upper crust where there are also some other sedimentary fills (SF) characterized by the *S*-wave speed ~2.6-2.7 km/s. The Kırşehir Massif – KM like the Menderes Massif – MM perturbed by the intrusions from the sub-crustal depths shows high speeds in the middle-to-lower crust (Çakır, 2018). The Anatolide-Tauride Platform (ATP) to the southeast of the ITSZ displays comparatively higher *S*-wave speeds (~3.6 km/s) and the positive VTI (around 9%) in the middle-to-lower crust and the negative VTI (around -10%) in the upper crust. The magmatic rocks with intra-plate to subduction- and collision-influenced affinity alongside the asthenospheric upsurge are frequent beneath the Anatolian plate and the inversion results (i.e., speed-anisotropy-depth distribution) herein support this observation (Dilek and Altunkaynak, 2007; Altunkaynak and Dilek, 2013; Nikogosian et al., 2018).

5. Discussions and Conclusion

The studied region is bordered by the IA(E)SZ to the south and the southern Black Sea cost to the north and the NAFZ and IPSZ run through the region in ~E-W direction (Figure 2). We have utilized the Love/Rayleigh dispersion curves (group and phase speeds – fundamental mode) to study the crust assemblage down to 40-km depth. The detected Love/Rayleigh dispersion data demonstrate *discrepancy*, i.e., isotropic model is not enough to describe the wave propagating medium. Anisotropic modeling (i.e., Vertical Transverse Isotropy – VTI) is found appropriate to model the detected dispersion data. The detected dispersion curves analogous to pathways between the source and receiver are converted to individual dispersion curves on a 0.1^o x 0.1^o sized grid making use of 2-D tomographic inversions. The checkerboard tests are performed to examine the effectiveness of the pathway's coverage of the existing surface wave data. Figure 3 demonstrates that the Love/Rayleigh group speed data can determine the lateral crust assemblages with size 0.50^o x 0.50^o or ~55 km resolve length. However, we see that there is still some confusion with the checkerboard patterns particularly to the E-SE where the inverted anomalies slightly mix with each other alongside the edges and corners. The Love/Rayleigh phase speed data have weaker pathways coverage and therefore the resultant resolution is coarser with larger size 0.65^o x 0.65^o or ~72 km resolve length (Figure 5). The inversion results revealed on the cross section (Figure 8) confirm the resolve length ~55 km chiefly governed by the group speed data.

Small-scale collections made of dykes and sills implanted in these anomalous assemblages act together to yield the detected VTI within the earth. One should note that the resolve length above emphasizes the resolve of the embedding assembly, but not the resolve of the small-scale (embedded) collection. The inversions reveal that under the Northwest and Central North Anatolia the small-scale collections in the middle-to-lower crust (i.e., horizontal sill assemblages) unusually slow down the Rayleigh surface waves (i.e., $V_{sh} > V_{sv}$) while another type of small-scale collections in the upper crust (i.e., vertical dyke assemblages) abnormally decelerates the Love surface waves (i.e., $V_{sv} > V_{sh}$). The mineral alignment in the magma flow within these small-scale collections acts to increment the detected VTI.

The suture zones populated by accretionary complexes and ophiolites may act like fault zones. They behave seismogenic creating earthquakes in the upper crust and flexible producing shear zones in the lower crust and may extend into the deeper lithospheric mantle. The current findings imply that the partially melted magma from the sub-crustal depths move upward to fill the gap between previous lithospheric plates for which the conforming magma intrusions develop as horizontal sill assemblages in the middle-to-lower crust creating the positive VTI. This magma emplacement is perhaps still cooling since the matching shear-wave speed is relatively low (i.e., V_s ~3.2 km/s). There are inner-suture-zone earthquakes with focal depths as deep as ~30-km, which is deeper than the fragile upper crust. These earthquakes principally in the lower crust may result from the upward magma movements within the suture zones. The partially melted magma is likely due to the uprising buoyant asthenosphere resulting from tearing, detachment, and erosion of the northerly Afro-Arabian slab beneath the Anatolian plate (Portner et al., 2018; Keskin, 2003; Biryol et al., 2011).

The general crust assemblage interpreted in terms of the V_s and η (Eq. 3) and earthquakes hypocenter distribution is shown to have six stratums including the half-space. The stratum boundaries demonstrate irregular fluctuations due to the perturbations by the vertical magma intrusions originating from the sub-Moho depths. The intrusions come forward as low speed (likely still cooling) and high speed (likely already cooled) zones. Depending on the physical circumstances the intrusions develop as either vertical dykes or horizontal sills. The Shape Preferred Orientation – SPO due to the dykes and sills and the Crystallographic Preferred Orientation – CPO due to the vertical and horizontal magmatic flows within the dyke/sill system yield the positive or negative Vertical Transverse Isotropy – VTI detected by the current surface wave data. The negative VTI results from $V_{sv} > V_{sh}$ and relates to the vertical dyke assemblages. On the other hand, $V_{sh} > V_{sv}$ yields the positive VTI and is associated with the horizontal sill assemblages.

The current findings are highlighted in the following list.

a) The suture zones [i.e., Izmir-Ankara-(Erzincan) Suture Zone – IA(E)SZ and Intra-Pontide Suture Zone – IPSZ] are typically identified as having Low Speed Zone – LSZ along with horizontal sill emplacement in the middle-to-lower crust in which there sometimes exist earthquakes as deep as 25-km focal depth perhaps in relation to contemporary magma flow with deeper origin, which is perhaps still in the process of cooling.

b) The other suture zone (i.e., Inner-Tauride Suture Zone – ITSZ) does not show signs as strong as shown by IA(E)SZ and IPSZ that can be used to find its location on the cross sections. The ITSZ mostly extends outside the frame that the current surface wave data covers and more data covering the Central Anatolian Volcanic Province as well as southern Anatolia should help better delineate the ITSZ.

c) Beneath the North Anatolian Fault Zone – NAFZ the uppermost crust is mostly characterized by low *S*-wave speed in the range 2.4-2.6 km/s due to the deformation zones filled with sedimentary deposits and the lower crust is categorized by high *S*-wave speed ~3.8 km/s due to the trans-tensional intrusions from the sub-Moho depths.

d) The Çankırı Basin – ÇB covering part of the Kırşehir Massif – KM to the north is categorized by the *S*-waves slowing down to ~2.5 km/s from ~2.8 km/s in the uppermost crust.

e) The Galatean Volcanic Province – GVP taking place between the IASZ and IPSZ does not demonstrate any specific feature on the cross sections in terms of the V_s and η that can be used to distinguish it from the nearby districts.

f) The Afyon Zone – AZ is categorized by intrusions from the sub-crustal depths causing HSZ in the lower crust, horizontal sill assemblage in the mainly middle crust and vertical dyke assemblage in the upper crust.

g) Beneath the Tavşanlı Zone – TZ the crust assemblage does not demonstrate significant VTI.

h) Beneath the Uludağ Massif – UM the crust assemblage is highly anisotropic. There exists vertical dyke in the lower crust as thick as 25-km in which the *S*-wave speed is ~3.8 km/s conforming to a propagating medium perhaps already cooled and the respective negative VTI is around -10%. This dyke is topped by horizontal sill in the middle crust with the respective positive VTI around 10%.

i) There exist some LSZs in the upper crust. The neighboring hot spring waters (GEOTERM, 2019) imply that these LSZs are still in the process of cooling.

j) The crust assemblage beneath the KM is relatively fast and show positive VTI mostly in the middle crust. The negative VTI in the lower crust is existent but relatively weak. These are also true for the Central Pontides – CP and Anatolide-Tauride Platform – ATP.

k) There exist earthquake accumulations in narrow regions which are likely activated by the neighboring upward magmatic intrusions causing local stress build-up near the surface.

Acknowledgement

We are grateful to the anonymous reviewers for critically reviewing the manuscript. We express our sincere gratitude to AFAD (Disaster and Emergency Management Presidency) for providing the accelerograms and to KOERI (Kandilli Observatory and Earthquake Research Institute) for providing the seismograms. We gratefully acknowledge the use of Generic Mapping Tool in figures. The accelerometer pole-zero files are kindly delivered by the instrument distributors.

Conflict of Interest

The author states that there is no conflict of interest.

References

Abgarmi, B., Delph, J.R. Özacar, A.A., Beck, S.L., Zandt, G., Sandvol, E., Turkelli, N., Biryol, C.B., 2017. Structure of the crust and African slab beneath the central Anatolian plateau from receiver functions: new insights on isostatic compensation and slab dynamics. Geosphere, 13(6), Pp. 1774–1787.

Adiyaman, Ö., Chorowicz, J., Arnaud, O.N., Gündogdu, M.N., Gourgaud, A., 2001. Late Cenozoic tectonics and volcanism along the North Anatolian Fault: new structural and geochemical data. Tectonophysics, 338(2), 2001, Pp. 135–165.

AFAD, 2019. Strong ground motion database of Turkey (TR-NSMN. Disaster and Emergency Management Presidency, Ankara, Turkey.

Akbaş, B., Akdeniz, N., Aksay, A., Altun, İ., Balcı, V., Bilginer, E., Bilgiç, T., Duru, M., Ercan, T., Gedik, İ., Günay, Y., Güven, İ.H., Hakyemez, H. Y., Konak, N., Papak, İ., Pehlivan, Ş., Sevin, M., Şenel, M., Tarhan, N.,Turhan, N., Türkecan, A., Ulu, Ü., Uğuz, M.F., Yurtsever, A., others, 2017. Geological map of Turkey. MTA (General Directorate of Mineral Research and Exploration of Turkey) Publications.

Akbayram, K., Okay, A., Satir, M., 2013. Early Cretaceous closure of the Intra-Pontide Ocean in western Pontides (northwestern Turkey. Journal of Geodynamics, 65(3), Pp. 38–55.

Alkan, H., Çınar, H., 2021. The lithospheric structure underneath the Circum Black Sea: Teleseismic receiver functions and Rayleigh wave phase velocity analysis, Journal of Asian Earth Sciences, 206, Pp. 104652.

Almqvist, B.S.G., D. Mainprice, D., 2017. Seismic properties and anisotropy of the continental crust: Predictions based on mineral texture and rock microstructure. Reviews of Geophysics, 55(2), Pp. 367–433.

Altunkaynak, Ş., Dilek, Y., 2013. Eocene mafic volcanism in northern Anatolia: its causes and mantle sources in the absence of active subduction. International Geology Review, 55(13), Pp. 1641–1659.

Bakırcı, T., Yoshizawa, K., Özer, M.F., 2012. Three-dimensional S-wave structure of the upper mantle beneath Turkey from surface wave tomography. Geophysical Journal International, 190(2), Pp. 1058–1076.

Biryol, B.C., Beck, S.L., Zandt, G., Özacar, A. A., 2011. Segmented African

lithosphere beneath the Anatolian region inferred from teleseismic P-wave tomography. Geophysical Journal International, 2011, 184(3), Pp. 1037–1057.

Çakır, Ö., 2018. Seismic crust structure beneath the Aegean region in southwest Turkey from radial anisotropic inversion of Rayleigh and Love surface waves. Acta Geophysica, 66(6), Pp. 1303–1340.

Çakır, Ö., 2019. Love and Rayleigh waves inverted for vertical transverse isotropic crust structure beneath the Biga Peninsula and the surrounding area in NW Turkey. Geophysical Journal International, 216(3), Pp. 2081–2105.

Çakır, Ö., Erduran, M., 2001. Effect of earth structure and source time function on inversion of single station regional surface waves for rupture mechanism and focal depth. Journal of the Balkan Geophysical Society, 4(4), Pp. 69–90.

Çakır, Ö., Erduran, M., 2011. On the P and S Receiver Functions Used for Inverting the One-Dimensional Upper Mantle Shear-Wave Velocities. Surveys in Geophysics, 32(1), Pp. 71–98.

Chanceaux, L., Menand, T., 2014. Solidification effects on sill formation: An experimental approach. Earth and Planetary Science Letters, 403(19), Pp. 79–88.

Confal, J.M., Faccenda, M., Eken, T., Taymaz, T., 2018. Numerical simulation of 3-D mantle flow evolution in subduction zone environments in relation to seismic anisotropy beneath the eastern Mediterranean region. Earth and Planetary Science Letters, 497(17), Pp. 50–61.

Çubuk-Sabuncu, Y., Taymaz, T., Fichtner, A., 2017. 3-D crustal velocity structure of western Turkey: Constraints from full-waveform tomography. Physics of the Earth and Planetary Interiors, 270(9), Pp. 90–112.

Delph, J.R., Biryol, C.B., Beck, S.L., Zandt, G., Ward, K.M., 2015. Shear wave velocity structure of the Anatolian Plate: anomalously slow crust in southwestern Turkey. Geophysical Journal International, 202(1), Pp. 261–276.

Dilek, Y., Altunkaynak, Ş., 2007. Cenozoic Crustal Evolution and Mantle Dynamics of Post-Collisional Magmatism in Western Anatolia. International Geology Review, 49(5), Pp. 431–453.

Dixit, M., Singh, A.P., Mishra, O.P., 2017. Rayleigh wave group velocity tomography of Gujarat region, Western India and its implications to mantle dynamics. Journal of Seismology, 21(4), Pp. 809–823.

Emre, Ö., Duman, T.Y., Özalp, S., Elmacı, H., Olgun, Ş., Şaroğlu F, 2013. Active faults map of Turkey (scale:1/1.125.000). MTA (General Directorate of Mineral Research and Exploration of Turkey) Publications, Ankara.

Fu, Y.V., Li, A., 2015. Crustal shear wave velocity and radial anisotropy beneath the Rio Grande rift from ambient noise tomography. Journal of Geophysical Research, 120(2), Pp. 1005–1019.

GEOSIG, 2012. Geosig, AC-73 triaxial force balance accelerometer. http://www.seismicsystems.net/images/pdfs/GS_AC-73_Leaflet_V12.pdf. Accessed 15 July 2019

GEOTERM, 2019. Geothermal areas in Turkey. Ministry of Energy and Natural Resources, Ankara, Turkey. https://www.enerji.gov.tr/tr-TR/Sayfalar/Jeotermal. Accessed 15 August 2019

Gök, R., Sandvol, E., Törkelli, N., Seber, D., Barazangi, M., 2003. Sn attenuation in the Anatolian and Iranian plateau and surrounding regions. Geophysical Research Letter, 30(24), Pp. 8042.

GURALP, 2013. Guralp systems, CMG-5TD digital accelerometer, operator's guide. https://www.guralp.com/documents/MAN-050-0005.pdf. Accessed 15 July 2019

Herrin, E., Goforth, T., 1977. Phase-matched filters: application to the study of Rayleigh waves. Bulletin of the Seismological Society of America, 67(5), Pp. 1259–1275.

Herrmann, R.B., 2002. Computer Programs in Seismology, version 3.30, St. Louis University, Missouri.

Hippolyte, J.-C., N. Espurt, N., Kaymakci, N., Sangu, E., Müller, C., 2016. Cross-sectional anatomy and geodynamic evolution of the Central Pontide orogenic belt (northern Turkey. International Journal of Earth Sciences, 105(1), Pp. 81-106.

İlkışık, O.M., 1995. Regional heat flow in western Anatolia using silica temperature estimates from thermal springs. Tectonophysics, 244(1–3), Pp. 175–184.

Kahraman, M., Cornwell, D.G., Thompson, D.A., Rost, S., Houseman, G.A., Türkelli, N., Teoman, U., Altuncu-Poyraz, S., Utkucu, M., Gülen, L., 2015. Crustal-scale shear zones and heterogeneous structure beneath the North Anatolian Fault Zone, Turkey, revealed by a high-density seismometer array. Earth and Planetary Science Letters, 430(22), Pp. 129–139.

Kaymakci, N., Özçelik, Y., White, S.H., van Dijk, P.M., 2009. Tectono-stratigraphy of the Çankiri Basin: Late Cretaceous to early Miocene evolution of the Neotethyan suture zone in Turkey, in Collision and Collapse at the Africa-Arabia-Eurasia Subduction Zone, edited by D. J. J. Hinsbergen et al. Geological Society, London, Special Publication, 311(1), Pp. 7–106.

Kendall, J.-M., 2000. Seismic anisotropy in the boundary layers of the mantle. In: Karato, S., Stixrude, L., Liebermann, R.C., Masters, T.G. Forte, A.M. (eds) Earth's Deep Interior: Mineral Physics and Tomography from the Atomic to the Global Scale, Geophysical Monograph Series, 117, American Geophysical Union, Pp. 149-175.

Kennett, B.L.N., Engdahl, E.R., 1991. Travel times for global earthquake location and phase association. Geophysical Journal International, 105(2), Pp. 429-465.

Keskin, M., 2003. Magma generation by slab steepening and breakoff beneath a subduction-accretion complex: An alternative model for collision-related volcanism in Eastern Anatolia, Turkey. Geophysical Research Letters, 30(24), Pp. 8046.

Kind, R., Eken, T., Tilmann, F., Sodoudi, F., Taymaz, T., Bulut, F., Yuan, X., Can, B., Schneider, F., 2015. Thickness of the lithosphere beneath Turkey and surroundings from S-receiver functions. Solid Earth, 6(3), Pp. 971–984.

Lee, S.-J., Kim, S., Rhie, J., Kang, T.-S., Kim, Y., 2021. Upper crustal shear wave velocity and radial anisotropy beneath Jeju Island volcanoes from ambient noise tomography, Geophysical Journal International, 225, Pp. 1332–1348.

Licciardi, A., Eken, T., Taymaz, T., Agostinetti, N.P., Yolsal-Çevikbilen, S., 2018. Seismic anisotropy in central north Anatolian Fault Zone and its implications on crustal deformation. Physics of the Earth and Planetary Interiors, 277(4), Pp. 99–112.

Mainprice, D., Nicolas, A., 1989. Development of shape and lattice preferred orientations: application to the seismic anisotropy of the lower crust. Journal of Structural Geology, 11(1–2), Pp. 175–189.

Menand, T., 2011. Physical controls and depth of emplacement of igneous bodies: A review. Tectonophysics, 500(1–4), Pp. 11–19.

Meschede, M., Warr, L.N., 2019. The Geology of Germany: Rocks and the Geological Record. Regional Geology Reviews, Pp. 9–18.

Miyazaki, T., Sueyoshi, K., Hiraga, T., 2013. Olivine crystals align during diffusion creep of Earth's upper mantle. Nature, 502(7471), Pp. 321–326.

MTA, 2002. Geological map of Turkey (scale:1/500000). MTA (General Directorate of Mineral Research and Exploration of Turkey) Publications, Ankara.

Nikogosian, I.K., Bracco Gartner, A.J.J., van Bergen, M.J., Mason, P.R.D., van Hinsbergen, D.J.J., 2018. Mantle sources of recent Anatolian intraplate magmatism: A regional plume or local tectonic origin? Tectonics, 37(12), Pp. 4535–4566.

Okay, A.I., 2008. Geology of Turkey: A synopsis. *Anschnitt*, 21(1), Pp. 19–42.https://web.itu.edu.tr/~okay/makalelerim/91_geology_of_turkey_anschnitt_2008.pdf

Okay, A.I., Tüysüz, O., 1999. Tethyan sutures of northern Turkey, In: Durand, B., Jolivet, L., Horváth, D., Sérranne, M. (eds) The Mediterranean basins: tertiary extension within the Alpine Orogen. Geological Society, London, Special Publications, 156(1), Pp. 475–515.

Özacar, A.A., Biryol, C.B., Zandt, G., Beck, S.L., 2006. North Anatolian Fault Passive Seismic Experiment: Receiver Functions along a Major Strike-Slip Fault, AGU Fall Meeting Abstracts.

Özdamar, Ş., Billor, M.Z., Sunal, G., Esenli, F., Roden, M.F., 2013. First U–Pb SHRIMP zircon and 40Ar/39Ar ages of metarhyolites from the Afyon–Bolkardag Zone, SW Turkey: Implications for the rifting and closure of the Neo-Tethys. Gondwana Research, 24(1), Pp. 377–391.

Pasvanoğlu, S., Çelik, M., 2019. Hydrogeochemical characteristics and conceptual model of Çamlıdere low temperature geothermal prospect, northern Central Anatolia. Geothermics, 79(3), Pp. 82–104.

Pasvanoğlu, S., Gültekin, F., 2012. Hydrogeochemical study of the Terme and Karakurt thermal and mineralized waters from Kirşehir Area, central Turkey. Environmental Earth Sciences, 66(1), Pp. 169–182.

Plunder, A., Agard, P., Chopin, C., Okay, A.I., 2013. Geodynamics of the Tavşanlı zone, western Turkey: Insights into subduction/obduction processes. Tectonophysics, 608(25), Pp. 884–903.

Portner, D.E., Delph, J.R., Biryol, C.B., Beck, S.L., Zandt, G., Özacar, A., Sandvol, E., Türkelli, N., 2018. Subduction termination through progressive slab deformation across Eastern Mediterranean subduction zones from updated P-wave tomography beneath Anatolia. Geosphere, 14(3), Pp. 1–19.

Pourteau, A., Oberhänsli, R., Candan, O., Barrier, E., Vrielynck, B., 2016. Neotethyan closure history of western Anatolia: a geodynamic discussion. International Journal of Earth Sciences, 105(1), Pp. 203–224.

Rawlinson, N., Sambridge, M., 2003. Seismic traveltime tomography of the crust and lithosphere. Advances in Geophysics, 46(1), Pp. 81–198.

SARA, 2017. Sara electronics instruments, SA10 force balance accelerometer. http://www.k-doit.com/?tpf=common/save_as&file_path=/attachment/201805&file_name=1525844823937739.pdf&orig_name=SA10_DATASHEET_ENG.pdf. Accessed 15 July 2019

Şengör, A.M.C., Yılmaz, Y., 1981. Tethyan evolution of Turkey: a plate tectonic approach. Tectonophysics, 75(3–4), Pp. 181–241.

Tang, Q., Zheng, C., 2013. Crust and upper mantle structure and its tectonic implications in the South China Sea and adjacent regions. Journal of Asian Earth Sciences, 62(1), Pp. 510–525.

Tarantola, A., 1987. Inverse Problem Theory, pp. 187–255, Elsevier Science Company Inc.

Topuz, G., Okay, A.I., 2017. Late Eocene–Early Oligocene two-mica granites in NW Turkey (the Uludağ Massif): Water-fluxed melting products of a mafic metagraywacke. Lithos, Pp. 268–271(1), 334–350.

Varol, E., Temel, A., Yürür, T., Gourgaud, A., Bellon, H., 2014. Petrogenesis of the Neogene bimodal magmatism of the Galatean Volcanic Province, Central Anatolia, Turkey. Journal of Volcanology and Geothermal Research, 280(11), Pp. 14–29.

Warren, L.M., Beck, S., Biryol, C., Zandt, G., Özacar, A., Yang, Y., 2013. Crustal velocity structure of Central and Eastern Turkey from ambient noise tomography. Geophysical Journal International, 194(3), Pp. 1941–1954.

Wenk, H.-R., Canova, G., Bréchet, Y., Flandin, L., 1997. A deformation-based model for recrystallization of anisotropic materials. Acta Materialia, 45(8), Pp. 3283–3296.

Wessel, P., Smith, W.H.F., Scharroo, R., Luis, J.F., Wobbe, F., 2013. Generic Mapping Tools: Improved version released. *EOS,* Transactions, American Geophysical Union, 94(45), Pp. 409–410.

Wilson, M., Tankut, A., Guleç, N., 1997. Tertiary volcanism of the Galatia province, north-west Central Anatolia, Turkey. Lithos, 42(1–2), Pp. 105–121.

Wu, T., Zhang, S., Li, M., Qin, W., Zhang, C., 2016. Two crustal flowing channels and volcanic magma migration underneath the SE margin of the Tibetan Plateau as revealed by surface wave tomography. Journal of Asian Earth Sciences, 132(18), Pp. 25–39.

Yıldırım, C., 2014. Relative tectonic activity assessment of the Tuz Gölü Fault Zone; Central Anatolia, Turkey. Tectonophysics, 630(17), Pp. 183–192.

Yolsal-Çevikbilen, S., Biryol, C.B., Beck, S., Zandt, G., Taymaz, T., Adıyaman, H.E., Özacar, A. A., 2012. 3-D crustal structure along the North Anatolian Fault Zone in north-central Anatolia revealed by local earthquake tomography. Geophysical Journal International, 188(3), Pp. 819–849.